Design and Numerical Characterization of a Low-Complexity Microwave Device for Brain Stroke Monitoring

Original
Design and Numerical Characterization of a Low-Complexity Microwave Device for Brain Stroke Monitoring / Scapaticci, R., Tobon, J., Bellizzi, G., Vipiana, F., Crocco, L.. - In: IEEE TRANSACTIONS ON ANTENNAS AND PROPAGATION. - ISSN 0018-926X. - STAMPA. - 66:12(2018), pp. 7328-7338. [10.1109/TAP.2018.2871266]

Publisher:
Institute of Electrical and Electronics Engineers Inc.

Published
DOI:10.1109/TAP.2018.2871266

Design and Numerical Characterization of a Low-Complexity Microwave Device for Brain Stroke Monitoring

Rosa Scapaticci, *Member, IEEE*, Jorge Tobon, Gennaro Bellizzi,
Francesca Vipiana *Senior Member, IEEE*, Lorenzo Crocco, *Senior Member, IEEE*

***Abstract*—This paper presents the design of a novel low-complexity microwave imaging system for monitoring brain stroke. In particular, the design is concerned with the determination of the optimal layout of the antennas array, namely minimum number, positions and polarization of the radiating elements, enabling the acquisition of an amount of data such to assure a reliable imaging. This goal is achieved by adopting a rigorous design procedure based on the inspection of the singular value decomposition of the relevant discretized scattering operator and taking into account the actual dynamics and signal to noise ratio of the measurement system. The design is first carried out in the case of ideal dipoles and then extended and assessed for actual printed monopole antennas, developed for the imaging system. The resulting system is a helmet equipped with 24 antennas, whose performances have been numerically validated in terms of both spatial resolution and reconstruction capabilities, by employing full-wave numerical simulations, realistic 3-D phantoms of the human head and an accurate modeling of the actual antennas employed in the system.**

***Index Terms*—microwave imaging, stroke monitoring, antennas.**

I. INTRODUCTION

BRAIN stroke is one of the most common cardiovascular diseases, with an incidence of about 15 million of cases every year worldwide, causing death or permanent injuries [1]. A brain stroke can be either ischemic (when one of the vessels of the brain is clogged) or hemorrhagic (when one of the vessel bursts) and its classification and imaging are very important to set the type of treatment. Therefore, diagnostic methodologies are of a great support to clinicians in choosing the therapy and in following its effectiveness.

Currently, the most adopted diagnostic tools are magnetic resonance imaging (MRI) and X-ray computerized tomography (CT). Although these techniques provide highly valuable diagnostic information, they are time-consuming (hence not able to provide real time images) and not portable (due to relevant size of the devices). In addition, CT is harmful due to ionizing radiations, whereas MRI is very expensive, so that they are unsuited for a continuous monitoring in ambulance or at bedside. For these reasons, there is an increasing interest in developing new diagnostic tools.

In this framework, microwave imaging (MWI) may represent an interesting alternative. In MWI, the imaging of the different brain tissues (stroke included) relies on their different response (i.e., electric contrast) to an applied microwave radiation, employed as probing stimulus [2], [3]. The stimulus is typically applied and collected through an array of antennas disposed around the head. The low intensities required by the microwave radiation makes this tool definitely safe. Moreover, by properly designing the antennas layout and the electronics, the imaging system can be made portable and cost-effective, hence, available at the patient bed or in ambulance for an almost real-time monitoring.

Currently, different microwave system prototypes for brain stroke diagnostics have been proposed in the literature.

The first and the most prominent example is the "Strokefinder", developed at Chalmers University [4], [5], which, however, is not meant for stroke imaging, but for its classification (ischemic or hemorrhagic). This device consists of 12 Tx/Rx triangular patch antennas mounted on a plastic helmet. Between the antennas and the head there are small plastic balloons filled with water, acting as matching medium. The stroke classification is performed by measuring the whole scattering matrix, over the frequency range 0.8-1.5 GHz, and processing the data through a machine-learning algorithm based on training, using data from patients with a known condition. In this device, number, positions and orientation of the antennas, as well as their distance from the head, are likely chosen mainly to better accommodate the antennas on the helmet.

A second system prototype is the one developed at the University of Queensland to image intracranial haematomas [6], [7]. This system consists of a ring of 16 corrugated and tapered slot antennas, operating in the frequency band 1-4 GHz (although only a smaller portion is used for imaging purposes). The antennas are in air and no matching medium is employed.

Manuscript received May 2017.

This work was supported by the Italian Ministry of University and Research (MIUR) under the PRIN project MiBraScan - Microwave Brain Scanner for Cerebrovascular Diseases Monitoring, and it has been also developed in the framework of COST Action TD1301, MiMed.

R. Scapaticci and L. Crocco are with the Institute for the electromagnetic sensing of the environment, national Research Council of Italy, 80124 Naples, Italy (email: {scapaticci.r,crocco.l}@irea.cnr.it).

J. Tobon and F. Vipiana are with the Department of Electronics and Telecommunications, Politecnico di Torino, 10129 Torino, Italy (email: francesca.vipiana@polito.it).

G. Bellizzi is with the Department of Electric Engineering and Information Technologies, Federico II University of Naples, 80125 Naples, Italy (email: gbellizz@unina.it).

Color versions of one or more of the figures in this paper are available online at http://ieeexplore.ieee.org.

Digital Object Identifier xxxxxxxxxxxxxxxxxxxx

The distance of neighboring antennas is chosen in order to have a mutual coupling lower than 20 dB over the band 1-4 GHz and the stroke imaging relies only on the monostatic data (i.e., the reflection coefficient at each antenna).

More recently, another system prototype has been developed, the ”BRIM G2” at EMTensor [8], which is meant for imaging purposes as well. This system consists of 177 ceramic-loaded rectangular waveguide antennas mounted on a semi-spherical stainless steel chamber. The antennas are evenly spaced on eight rings, at different heights. The working frequency is 1 GHz. The employed matching medium is a mixture of glycerin and water. The large number of antennas employed in this system is set to be likely sure to acquire all the available information content for imaging purposes. However, this has some obvious drawbacks, at least in terms of cost and portability of the system.

The aim of this paper is to design and assess a novel, low-complexity, microwave imaging system for continuously monitoring brain stroke in the post-acute stage. Proper follow-up after the onset is crucial to improve the recovery of the patient and represents an unmet clinical need, owing to the aforementioned limitations of MRI and CT. Moreover, MWI is particularly suited to pursue this diagnostic goal. As a matter of fact, the variation of the electric contrast due to the stroke evolution is sufficiently small and localized. Consequently, the imaging problem can be reduced to a linear (ill-posed) inverse problem. This is a key feature, as this allows the system to provide real-time images, through ad-hoc inverse scattering based data-processing techniques [9], [10] and their proper hardware implementation.

Of course, to turn the advantage of differential imaging into practice, it is necessary that the intended variation truly occurs only in the target of the survey (i.e., the possible changes in the tissue affected by the stroke). This requirement calls for a proper realization of the helmet and the identification of practical rules for its positioning in a way as much repeatable as possible. On the other hand, a previous study concerned with the imaging algorithm herein exploited has shown that such an algorithm is robust against reasonable misalignment errors (e.g., in the order of one centimeter) [10].

The study presented in the following is concerned with the determination of the optimal layout of the antennas array, namely minimum number, position and polarization of the radiating elements enabling the acquisition of an amount of information content such to assure a reliable imaging has been determined. Then, the performances of the designed system have been assessed in terms of spatial resolution and reconstruction capabilities, by employing full-wave 3-D numerical simulations, realistic phantoms of the human head and an accurate modeling of the actual antennas that will be employed in the system.

As compared to the existing devices described above, the proposed device differs for the specific imaging goal (e.g., monitoring the stroke evolution after its onset) and, more important, for the adoption of a rigorous design procedure, rather than empirical rules or practical considerations. In particular, previous, experimentally validated, findings [9], [11] have been exploited to fix the working environment (e.g., operating frequency and coupling medium), whereas a recently proposed rigorous procedure has been exploited to design the array layout [12]. Such a procedure is based on the quantitative analysis of the singular value decomposition (SVD) of the discretized scattering operator [13] and is herein particularized to the case of data acquired by antennas located on a surface conformal to the head (a helmet), taking into account the actual dynamic range and signal to noise ratio (SNR) of the measurement system and the effective size of the employed antennas. The adopted design procedure allows to identify a low-complexity 24 elements array as the suitable candidate to perform the sought imaging task and the expected performances are confirmed by the performed numerical analysis.

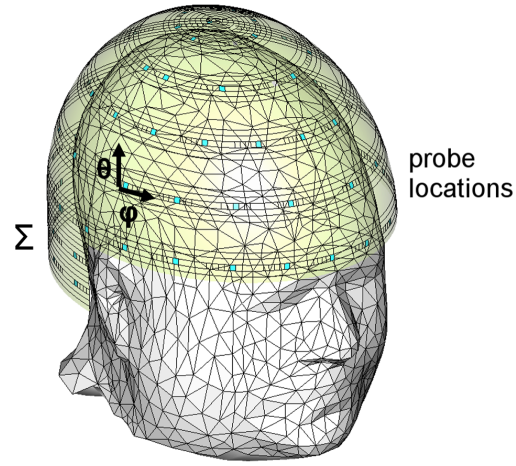

Fig. 1. Selected positions (blue points) and orientations (black arrows) of the probes (ideal elementary dipoles) on the scanning surface Σ.

The remaining part of the paper is organized as follows. The theoretical background is given in Section II. The design of the optimal antenna array layout will be provided in Section III. In Section IV, the performance of the system in terms of spatial resolution have been assessed first by assuming elementary dipoles as array elements and then by considering an *ad hoc* designed antenna. Finally, in Section V a realistic imaging example is presented, in which a hemorrhagic stroke is simulated in an anthropomorphic 3-D phantom of the human head and where an accurate modeling of the actual antennas adopted in the system is performed by means of full-wave numerical simulations. Preliminary numerical results related to this paper have been presented in a conference communication [14], and in the framework of a larger study discussing the feasibility of microwave imaging as diagnostic modality for brain imaging [11].

II. THEORETICAL BACKGROUND

Fig. 1 shows a sketch of the radiating part of the MWI system under development. Each antenna radiates an almost linearly polarized field (see Section IV) and acts both as transmitter (Tx) and receiver (Rx). The antennas are tangentially disposed onto a helmet whose shape is conformal to the upper part of the head. The helmet also acts as a holder for the matching medium, inserted between the head and the antennas, in order to reduce the mismatch at the skin interface.

The working frequency band and the matching medium permittivity are chosen in order to guarantee the best trade-off between wave penetration inside the head and imaging resolution. According to the findings in [9], experimentally confirmed in [11], the best compromise is achieved by exploiting the narrow working frequency band 0.8-1.2 GHz, centered at f=1 GHz, and a matching medium with relative permittivity ϵ_b around 20, with a conductivity as low as possible. Such permittivity value can be practically obtained in different ways, such as, for instance, by means of proper mixtures of Triton X-100 and water [15], [16].

The distance between the conformal surface and the head is set about 2.5 cm, corresponding to about 0.4 times the wavelength (λ) at the center frequency (f=1 GHz) in the chosen matching medium. Such choice is motivated by the necessity of having a compact device, in which the low useful signals are not too much attenuated, while, at the same time, minimizing near field effects which are hard to be modeled properly and only marginally contribute to the reconstruction of the interior portion of the imaged domain (which is herein of interest) [17].

According to [12], to determine the optimal array layout the first step is to provide the expression of the relevant scattering operator, relating the unknown contrast variation, due to the stroke evolution, to the measured data. To this end, let us assume that the imaging of the stroke is performed by measuring the multi-static, multi-view scattering matrix, whose generic p,q-th entry is the signal scattered by the head and measured by the p-th antenna of the array (when operating in Rx mode), due to the impinging field radiated by the q-th antenna of the array (when operating in Tx mode).

As a matter of fact, since we are interested in monitoring the time evolution of the stroke after its onset, hence the electric contrast variation of the brain tissue at two different monitoring times, the data actually processed are given by the difference between the scattering matrices measured at these two different times (differential imaging).

Now, such differential data, denoted with ΔS, have the following expression:

$$\Delta S\left(\boldsymbol{r}_p, \boldsymbol{r}_q\right) = \frac{-j\omega\epsilon_b}{4} \int_D \boldsymbol{E}_{\mathrm{b}}\left(\boldsymbol{r}_p, \boldsymbol{r}\right) \cdot \boldsymbol{E}\left(\boldsymbol{r}, \boldsymbol{r}_q\right) \Delta\chi\left(\boldsymbol{r}\right) d\boldsymbol{r}. \tag{1}$$

In (1), D is the region of interest (ROI), i.e., the head, $\boldsymbol{r}_p$ and $\boldsymbol{r}_q$ the positions of the Rx and Tx antennas (with respect to a fixed reference frame) on the measurement surface, say Σ, $\omega = 2\pi f$ is the angular frequency, j the imaginary unit, $\Delta\chi\left(\boldsymbol{r}\right)$ is the electric contrast variation due to the time evolution of the stroke in the ROI, $\boldsymbol{E}_{\mathrm{b}}\left(\boldsymbol{r}_p, \boldsymbol{r}\right)$ the "background" electric field, radiated in the ROI by the antenna located at $\boldsymbol{r}_p$ when $\Delta\chi\left(\boldsymbol{r}\right) = 0$, and $\boldsymbol{E}\left(\boldsymbol{r}, \boldsymbol{r}_q\right)$ the total field in the ROI due to the antenna located at $\boldsymbol{r}_q$, given by the superposition of the incident field $\boldsymbol{E}_{\mathrm{b}}\left(\boldsymbol{r}, \boldsymbol{r}_q\right)$ (independent of $\Delta\chi$) and the resulting field scattered by $\Delta\chi$. In (1) the symbol "$\cdot$" denotes the dot product between vectors. Notably, in addition to the antenna position, ΔS also depends on the antenna polarization and orientation on Σ.

In typical circumstances, the differential contrast $\Delta\chi$ is localized in a small portion of the ROI, wherein the variation of the stroke is occurring. Accordingly, it is possible to take advantage of the distorted Born approximation, and to assume that $\boldsymbol{E}\left(\boldsymbol{r}, \boldsymbol{r}_q\right) \cong \boldsymbol{E}_{\mathrm{b}}\left(\boldsymbol{r}, \boldsymbol{r}_q\right)$. Accordingly, (1) becomes linearly dependent on $\Delta\chi$ and (1) can be rewritten in a compact fashion as:

$$\Delta S\left(\boldsymbol{r}_p, \boldsymbol{r}_q\right) = \mathcal{S}\left(\Delta\chi\right), \tag{2}$$

where $\mathcal{S}$ is a linear and compact integral operator relating the data ($\Delta S\left(\boldsymbol{r}_p, \boldsymbol{r}_q\right)$) to the unknown of the problem ($\Delta\chi$), whose kernel is $-j\omega\epsilon_b/4 * \boldsymbol{E}_{\mathrm{b}}\left(\boldsymbol{r}_m, \boldsymbol{r}_p\right) \cdot \boldsymbol{E}_{\mathrm{b}}\left(\boldsymbol{r}_m, \boldsymbol{r}_q\right)$.

Ideally, $\mathcal{S}$ is defined on a continuous scanning/measurement surface, i.e., $\boldsymbol{r}_p$ and $\boldsymbol{r}_q$ can assume all the possible positions on Σ. In practice, one can deal only with a discrete version of problem (2). Hence, denoting with N the number of Tx/Rx antennas and with M the number of sub-domains wherein ROI is discretized, in its discrete form (2) becomes:

$$[y] = [S_d] \cdot [x], \tag{3}$$

where $[y]$ is the N^2 column vector of the measured values of $\Delta S\left(\boldsymbol{r}_p, \boldsymbol{r}_q\right)$, $[x]$ the M column vector whose m-th entry is $\Delta\chi\left(\boldsymbol{r}_m\right)$ with $\boldsymbol{r}_m \in D$, $[S_d]$ the $N^2 \times M$ matrix whose generic entry is $-j\omega\epsilon_b/4 * \boldsymbol{E}_{\mathrm{b}}\left(\boldsymbol{r}_m, \boldsymbol{r}_p\right) \cdot \boldsymbol{E}_{\mathrm{b}}\left(\boldsymbol{r}_m, \boldsymbol{r}_q\right)$. Note that, due to the reciprocity, $S\left(\boldsymbol{r}_p, \boldsymbol{r}_q\right) = S\left(\boldsymbol{r}_q, \boldsymbol{r}_p\right)$, the size of $[y]$ and $[S_d]$ in (3) is reduced from N^2 to $L = N(N+1)/2$.

In (3), $[y]$ is the data while $[x]$ is the unknown; the matrix $[S_d]$ is exactly known once the reference electric scenario of the ROI, i.e. the scenario when $\Delta\chi\left(\boldsymbol{r}\right) \equiv 0$, is known and can be computed by numerical simulations. Unfortunately, the latter information is patient-specific and time-dependent (due to the stroke evolution). However, in [10], [12] it has been shown that both the design of an optimal imaging system and the development of an effective imaging strategy can be obtained by assuming as reference scenario the one having the same shape of ROI, but filled with a homogeneous medium. In the following we will make use of this assumption, taking as "background field" the one radiated in a homogeneous head having relative permittivity equal to the average among the different tissue in the head.

III. OPTIMAL ANTENNA ARRAY LAYOUT DESIGN

Hereinafter, if not differently specified, we will consider elementary electric dipoles oriented tangentially to Σ as radiating elements. Note this is the most generic possibility, since the field radiated by any real antenna can be expressed as superposition of the fields radiated by elementary dipoles.

The design procedure is based on the inspection of the SVD of the operator in (2) as $\mathcal{S} = [u] \cdot [\sigma] \cdot [v]^T$ [12].

First, we have evaluated the condition number (CN) of $[S_d]$, given by the ratio between the first (i.e., the largest) and the last (i.e., the smallest) singular value of $[S_d]$. CN is a direct measure of the ill-conditioning of the problem (3). Therefore, the smaller CN is, the more robust the inversion of (3) is against the measurement noise on the data and modeling error.

Figure 2 shows CN (in dB) of $[S_d]$ for different values of the number of probes, N_d, and orientation of the probes (along

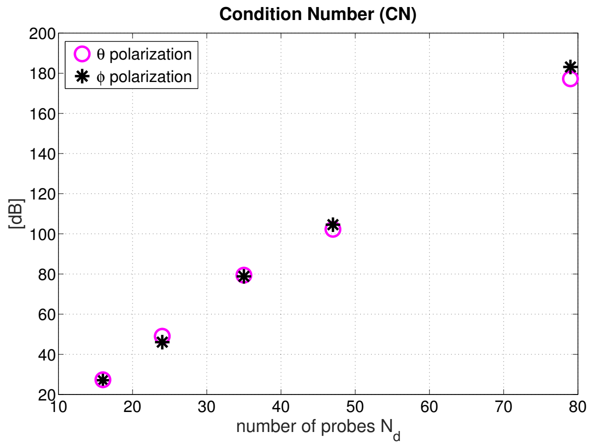

Fig. 2. Condition number of the discretized scattering operator versus the number and orientation of the probes on Σ (probes evenly spaced on Σ).

either θ (vertical) or ϕ (horizontal) directions in Fig. 1 on Σ). In all cases, the probes are approximately equally spaced on Σ. As it can be seen, whatever the probe orientation, CN increases by increasing N_d. This is of course an expected result and is due to the fact that the information content gathered by probes which are very close to each other is strongly dependent, while the measurement noise is always almost independent.

Interestingly, for a reasonable number of probes, i.e., $N_d =$ 16, 24 and 31, a relatively small CN is obtained, remarkably lower than the dynamics and the SNR of a standard measurement system (which can be considered around 90 dB); CN increases above this threshold for $N_d = 48$. Also, from Fig. 2, it is possible to state that the ϕ or θ orientation are basically equivalent.

According to this first analysis, an optimized MWI system should not have a number of probes larger than 48 in order to assure a stable image reconstruction against measurement noise and modeling errors. Of course, the smaller is the number of probes the more stable is the reconstruction. On the other hand, a small number of probes also translates in a reduced reconstruction accuracy, due to the loss in terms of collected information, caused by the loose discretization of the continuous operator. In this respect, an optimal design of a MWI system has to address a good trade-off between stability (dictated by the conditioning of the problem) and accuracy, which is in turn dictated by the discreatization of the continuous operator $\mathcal{S}$.

To quantify this aspect as an effect of the translation from a continuous (ideal) scanning surface to a finite number of antennas, let us consider the discretization error ϵ_S [12]:

$$\epsilon_S = \frac{\|[S] - [S] \cdot [\Pi_{N_d}]\|}{\|[S]\|}, \tag{4}$$

where the symbol "$\|\ \|$" denotes the matrix norm and the matrix $[\Pi_{N_d}]$ is defined as:

$$[\Pi_{N_d}] = [S_d]^+ \cdot [S_d] = \sum_{n=1}^{N_d} [v_n] \langle \ \cdot \ , [v_n] \rangle \tag{5}$$

where $[S_d]^+$ is the pseudo inverse of $[S_d]$ and $[v_n]$ the right singular vectors of $[S_d]$.

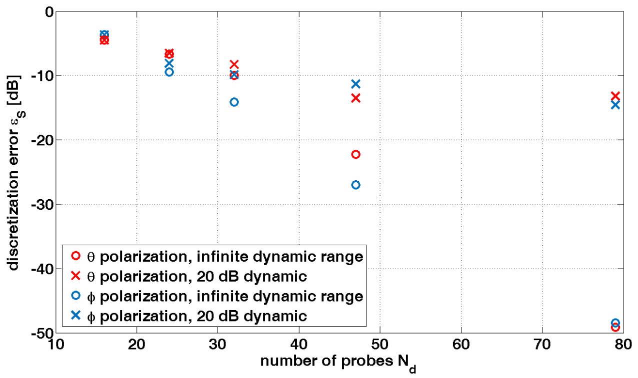

Fig. 3. Discretization error for a different number and orientation of the antennas/probes, evenly spaced on Σ, and for an infinite or limited (20 dB) dynamic range of the system.

Note that $[\Pi_{N_d}]$ represents the orthogonal projection onto the finite dimensional space of the contrast functions spanned by the first N_d right singular vectors $[v_n]$ of $[S_d]$. Such space represents the set of all possible contrasts $[x]$ that can be reconstructed from a finite number, N_d, of Tx/Rx probes on the scanning surface Σ. Of course, such subspace depends not only on N_d, but also on the position and orientation of the dipoles on Σ. As a result, ϵ_S gives a measure of the distance, in the relevant functional space, between the actual contrast and the contrast which can be reconstructed by using a limited number of antennas. As such, it measures the accuracy of the "ideal" reconstruction. It can be foreseen the general trend that the larger is N_d the lower is ϵ_S. Moreover, ϵ_S changes by changing either the antenna positions or the orientation on Σ. Now, let us note that the differential signal (i.e., the one due to the stroke variation) is typically about 70 dB below those measured at two monitoring times (which are due to the scattering from the whole head) [10]. On the other hand, considering that the measurement part of the developed MWI system has a limited dynamic range (DR) of about 90 dB (which is actually a conservative assumption since modern instrumentation exhibit a DR above such value), the actual DR available for the differential signal is around 20 dB. This means that all the components $[v_n]$ of $[x]$, in (5), whose singular value σ_n is 20 dB below the highest one, σ_1, cannot be accurately reconstructed due to the finite DR of the system. To take into account such limitation of the available accuracy, the orthogonal projector in (5) can be replaced with its "limited accuracy" version obtained by truncating the summation in (5) at the index $N_{\mathrm{DR}} < N_d$ corresponding to the number of singular values of $[S_d]$ not lower than 20 dB the highest one, σ_1. Typically, $N_{\mathrm{DR}} \ll N_d$.

Figure 3 shows ϵ_S evaluated for an increasing number of probes N_d, equally spaced on Σ, and different polarizations of the antennas (i.e., along either θ or ϕ directions in Fig. 1) both for an infinite and limited (20 dB) DR. The continuous operator $\mathcal{S}$ appearing in (4) was computed by considering about 180 probes, which largely exceeds the number required to sample the surface Σ at the Nyquist rate.

From Fig. 3, one can note that ϵ_S for the ϕ (horizontal) and θ (vertical) polarization are almost equivalent, only slightly lower for the ϕ polarization. Moreover, for the actual case of a limited accuracy, the improvement in ϵ_S when increasing the number of probes becomes negligible from 24 to 48 antennas, while it corresponds to a remarkable increase of both the CN and the hardware complexity. A higher error, instead, is obtained with the configuration with 16 probes. A good compromise could be 24.

IV. Imaging performance analysis

To consolidate the above design guidelines, we have evaluated the point spread function (PSF) of the discretized operator $[S_d]$ to assess the actual spatial resolution achievable with the designed array (made of ideal probes). The PSF has been evaluated by applying the orthogonal projection operator in (5) to a point like contrast variation $\Delta\chi$. According to the above results, the analysis has been performed by assuming the ϕ (horizontal) orientation for the probes and by changing their number N_d and the effective available DR for the differential signal. In all cases the probes are almost evenly distributed on Σ.

The results are shown in Fig. 4 for three orthogonal axes crossing the point-like contrast, built by selecting one single tetrahedron of the mesh (located at (0.038; 0.0402; 0.0829) m) and setting $\Delta\chi$=1 for this tetrahedron, while setting $\Delta\chi$=0 for all the other tetrahedra. Specifically, Figs. 4.a-c show the PSF for a different number of probes and fixing the DR at 40 dB.

To quantitatively appraise the performance of the imaging system from its PSF, the resolution and the side lobe level (SLL) have been evaluated. The resolution is calculated as the width of the main lobe at -3 dB and it indicates how a point-like target is filtered and spread from the imaging system at hand. The SLL is the amplitude (in dB of the normalized reconstruction) of the largest lobe after the main one and it is a metric that quantifies the possibility of distinguishing the reconstruction of the target from spurious artifacts. The values of the adopted metrics are reported in Table I, from which one can note that the obtained resolution is around $\lambda/4$ (λ being equal to 6.5 cm), in agreement with theoretical forecast of linearized MWI [18]. The second important observation is that the major loss of resolution occurs along the z-axis. This is certainly due to the fact that the measurement surface is "truncated" (i.e., it is not closed) along the z-axis. Last, the width of the main lobe, hence the spatial resolution, increases as expected by reducing the number of probes, but the gain in resolution moving from 24 to 79 probes is not significant, as it is less than 5 mm, while a not negligible worsening of the resolution along the x-axis as well as of the SLL is observed for the configuration with only 16 probes. These considerations allow to conclude that, as suggested by the analysis in the previous section, the 24-antennas layout represents the best compromise between stability, accuracy, spatial resolution of the reconstruction, hardware complexity and overall cost of the MWI system. Finally, to observe the effect of the dynamics, panels d-f of Figs. 4 report the PSF for 24 probes for different DR values, from 20 to 40 dB. From this analysis one can note that the resolution remains essentially unchanged while varying the DR (but for a slight loss of resolution limited to the z-axis when DR is downed at 20 dB).

TABLE I
IMAGING RESOLUTION USING IDEAL PROBES AND $40dB$ OF DYNAMICS.

Number of probes	axis	lobe width [cm]	SLL [dB]
79	x-axis	1.46	-17.7
	y-axis	1.60	-23.2
	z-axis	1.70	-20.7
47	x-axis	1.53	-17.2
	y-axis	1.60	-21.7
	z-axis	1.65	-19.6
35	x-axis	1.66	-21.4
	y-axis	1.65	-23.4
	z-axis	1.75	-18.9
24	x-axis	1.73	-24.4
	y-axis	1.70	-25.6
	z-axis	1.95	-21.9
16	x-axis	2.00	-14.2
	y-axis	1.80	-17.7
	z-axis	2.00	-23.3

A. *From elementary probes to real antennas*

So far, the analysis has been carried out considering ideal dipole antennas. This is of course different from the actual situation, wherein real antennas are employed and coupling between them occurs, possibly changing the overall behaviour of the system. Accordingly, we have repeated the analysis to assess the effect of the antenna coupling on the PSF, hence on the spatial resolution. In particular, we have repeated the analysis in Figs. 4.d-f by replacing in the simulation the ideal dipoles with the antennas actually employed in the MWI system [14]. The implemented antennas are wide-band monopole antennas printed on a standard FR4 dielectric substrate with thickness 1.6 mm. The antenna has been designed to have a good matching in the considered bandwidth, when the antenna is immersed in the coupling medium, and to minimize its dimensions so to accommodate 24 antennas around the upper part of the head (as shown in Fig. 5). The final antenna size is 3 x 4 cm where, on upper side of the FR4 substrate, the radiating part with triangular shape and the feeding line are printed, while, on the lower side, behind the feeding line, there is the ground plane.

Note that, the adopted coupling medium has been chosen in such a way to maximize (at the operating frequency) the matching between the incoming signal and the head (or equivalently minimize the reflection at the head surface), while considering the non-homogeneous nature of the latter [9]. As a consequence, the antennas "see" a low discontinuity and are expected to work in conditions which are almost the same as those in which they have been designed.

As a proof to this ansatz, figure 6 shows the antenna geometry and the simulated $|S_{11}|$ (dB) of the antenna immersed in the coupling medium, in presence of a homogeneous head filled with white matter and in presence of an actual head. As can be seen, no significant variation of the $|S_{11}|$ can be observed by changing the scenario in which the antenna has been designed. We have also studied (and omitted herein for brevity) the distribution of the electric field radiated by one

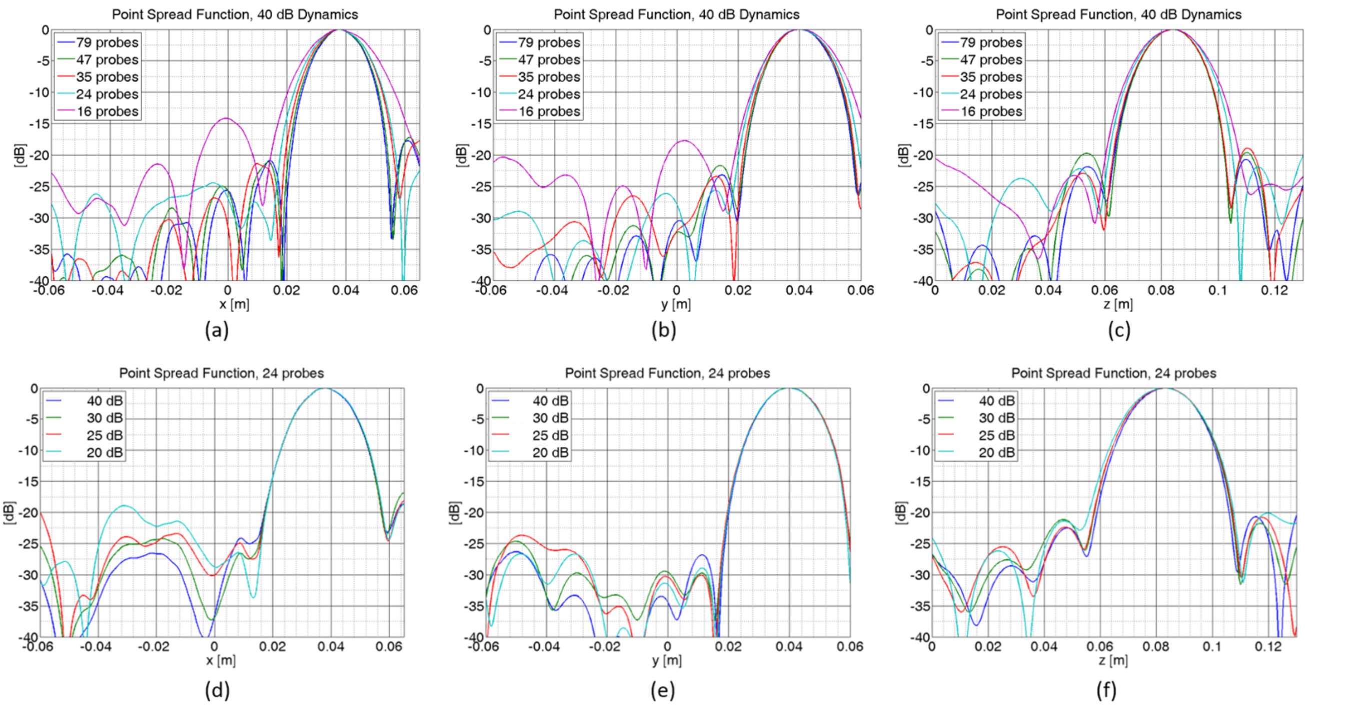

Fig. 4. Point spread function of the discretized scattering operator evaluated along three orthogonal axis intersecting the stroke. Panels (a)-(c) show the PSF for a different number of (ideal) probes, oriented along the ϕ direction, evenly spaced on Σ, and a fixed dynamic range of 40 dB. Panels (d)-(e) show the PSF for 24 (ideal) probes, oriented along the ϕ direction, evenly spaced on Σ, and different dynamic ranges.

antenna in the same three cases confirming, given the coupling medium, the scarce dependence of the antenna behavior with respect to the scenario at hand.

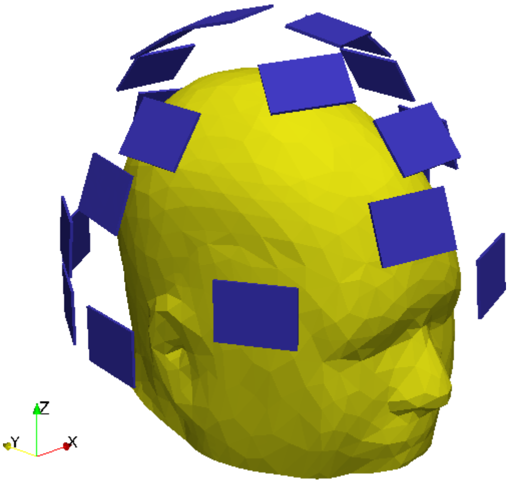

Fig. 5. Realistic antennas around head.

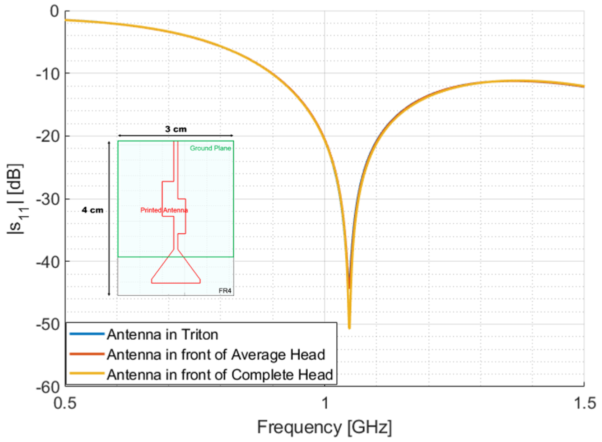

Fig. 6. Simulated reflection coefficient at the antenna port when the antenna is immersed in proposed matching liquid. Geometry and dimensions of the antenna are depicted in insert.

The results of the PSF with the real antennas are reported in Fig. 7, while the resolution and SLL values are reported in Table II. From the comparison of the results of Fig. 4d-e with Fig. 7 and Table I with Table II, one can note that there is a slight broadening of the main lobe of PSF. This can be ascribed to the antenna coupling, neglected in the previous analysis involving elementary dipoles and now taken into account. The reason of such a worsening of the imaging capability is that the coupling changes the space of contrast spanned by the first N_{DR} right singular vectors of the discretized scattering operator $[S_d]$, thus changing the kind of contrast functions actually retrievable. In any case, the broadening decreases by increasing the DR and this suggests that by increasing the DR, hence N_{DR}, the the singular vectors, in the case of ideal and real antennas,span the same space. From the results in Fig. 7, the effect of the coupling becomes negligible for a DR of 40 dB. This means that, for a device of 24 antennas, the acquisition system must be characterized by a higher overall DR to achieve the same resolution as in the case of ideal probes.

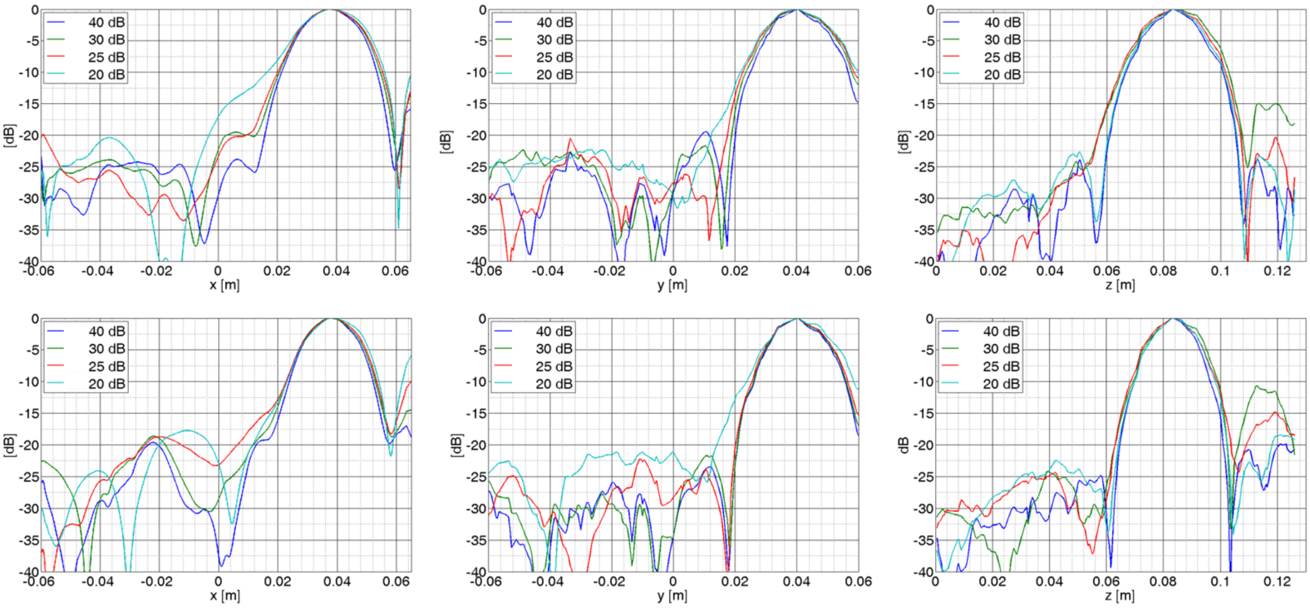

Fig. 7. Point spread function of the discretized scattering operator evaluated for 24 printed monopole antennas, oriented along the ϕ direction, evenly spaced on Σ, and different dynamic ranges. Top row: scattering operator computed in the homogeneous background medium; bottom row: scattering operator computed in a scenario made of a head filled with homogeneous white matter immersed in the background medium.

TABLE II
IMAGING RESOLUTION USING REAL ANTENNAS AND DIFFERENT DYNAMICS.

DR [dB]	axis	lobe width [cm]	SLL [dB]
40	x-axis	1.89	-23.9
	y-axis	1.65	-19.4
	z-axis	1.65	-23.8
30	x-axis	2.02	-19.5
	y-axis	1.85	-21.7
	z-axis	1.8	-18.7
25	x-axis	2.07	-19.9
	y-axis	1.95	-20.5
	z-axis	2.05	-20.3
20	x-axis	2.21	-20.4
	y-axis	2.00	-22.3
	z-axis	2.05	-15.0

It is worth noting how the results obtained for the resolution and the SLL are almost independent of the stroke position in the brain. To confirm such an expectation, we have evaluated the performance of the designed imaging system, with respect to an "average scenario", built as an homogeneous head having electric properties of white matter. This is indeed, the reference scenario actually exploited in the imaging procedure presented in next section [10]. In this analysis, we have computed the PSF of the imaging system in a large number of points (57), randomly selected inside the region occupied by the brain, as can be seen from Fig. 8. The mean values and standard deviation of both resolution and SLL are reported in Table III, which show a slight increase of the lobe width, and a SLL consistent with the one observed in the previous analysis on a single point.

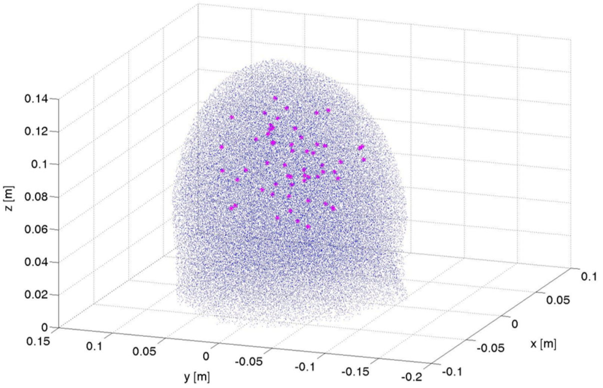

Fig. 8. 57 randomly selected points inside brain region.

TABLE III
STATISTICAL ANALYSIS ON IMAGING RESOLUTION USING REAL ANTENNAS AND DR = $20dB$.

axis	lobe width [cm]		SLL [dB]	
	Mean	std	Mean	std
x-axis	1.89	0.31	-12.2	5.5
y-axis	2.50	0.69	-16.2	5.4
z-axis	2.43	0.33	-18.1	16.1

V. NUMERICAL EXAMPLE ON REALISTIC PHANTOM

To give an example of the imaging capabilities of the designed MWI system layout with respect to a realistic anthropomorphic scenario, a numerical experiment has been set up.

As head phantom, we have employed the 3D realistic model in [19], extracted from MRI data. Figure 9 shows the internal structure of the head phantom along three orthogonal cuts;

Table IV lists all the tissue included in the phantom and the values of their electric properties at the work frequency of 1 GHz [20].

The antennas are embedded in a matching medium having $\epsilon_r = 23.130$ and $\sigma = 0.335$ S/m, at 1 GHz (loss tangent equal to $tan\delta$ = 0.26). Such an medium can be built through a 70%-30% Triton x-100 -Water mixture [15] and represents a good trade-off between imaging resolution and attenuation of the EM fields due to losses.

To simulate the presence of a hemorrhagic stroke, we have included in the head model a spherical region having the dielectric properties of blood ($\epsilon_r = 61.065$ and $\sigma = 1.583$ S/m at 1 GHz), at two different positions: inside the grey matter (position 1) and inside the white matter (position 2). To simulate the stroke evolution at two different monitoring instants, t_1 and t_2, for each position, we have considered a stroke with two different radii: 1 cm (at t_1) and 2 cm (at t_1) - see fig. 10. The data processed by the inversion algorithm are given by the difference of the scattering matrices measured at t_1 and t_2 (differential imaging). The adopted reconstruction algorithm is a truncated SVD based scheme, in which the problem in (3) is solved via the inversion formula:

$$[x] = \sum_{n=1}^{L_t} \frac{1}{\sigma_n} \langle [y], [u_n] \rangle [v_n] \tag{6}$$

where $[y]$ is the differential data matrix, $\langle [u], [\sigma], [v] \rangle$ is the SVD of the discretized scattering operator, herein built with respect to an average scenario represented by a homogeneous head with properties of the white matter immersed in the adopted coupling medium. $L_t < L$ acts as regularization parameter and is set in order to have a satisfactory trade-off between stability of the reconstruction (with respect to noise on data and modeling errors arising from the adopted reference scenario) and accuracy of the resulting image (in terms of spatial resolution). A good compromise is achieved by setting the truncation index to a value which is slightly larger than the one corresponding to the change of slope (knee) of the singular value behavior [13], in this case at $L_t = 63$. It is worth noting that the adopted reconstruction algorithm described above is very robust against errors on the antenna positioning [10].

TABLE IV
CHARACTERISTICS AT 1 GHZ FOR MATERIALS USED IN NUMERICAL TEST.

	Material	ϵ_r	σ [S/m]
1	Fat	5.447	0.053
2	Gray Matter	52.282	0.985
3	White Matter	38.577	0.622
4	Cerebellum	48.858	1.308
5	Bone (Skull)	12.363	0.156
6	CSF	68.439	2.455
7	Skin	40.936	0.089

All the full-wave simulations have been performed with an in-house vectorial 3D Finite Element Method (FEM) [21]. The volume has been meshed into tetrahedral elements achieving a good description of the realistic geometries. On the other hand, in order to build the scattering operator $[S_d]$ to be inverted, an interpolation on cartesian coordinates has been performed.

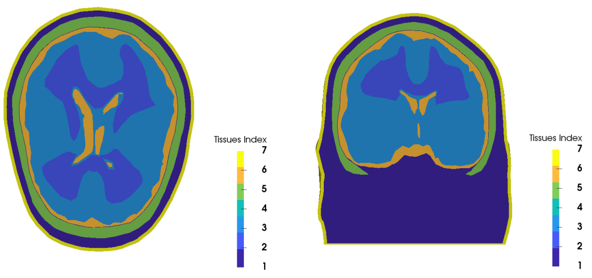

(a) Transverse plane (b) Frontal plane

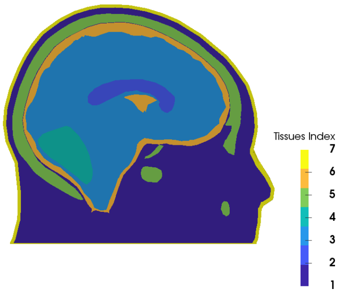

(c) Sagittal plane

Fig. 9. Numerical phantom. Indexes refer to tissues in table IV

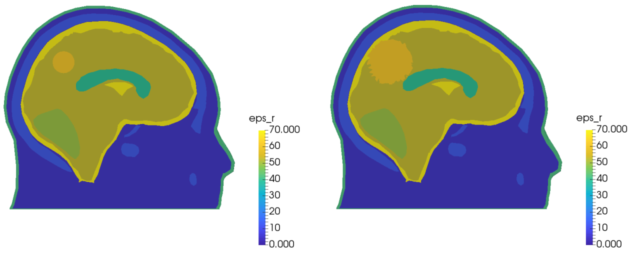

(a) Stroke at T1 (b) Stroke at T2

Fig. 10. Sagittal plane for scenario with stroke at position 1 in two different instants. ϵ_r at 1 GHz values displayed.

Synthetic data have been corrupted by an additive Gaussian noise with two different levels, i.e., $SNR = 90$ dB and $SNR = 80$ dB. Independent noise has been added to the data gathered at each considered time instant and then differential data have been obtained from noisy scattering matrices. Note that the differential signal is quite low, compared to the total measured one. We can evaluate its intensity by comparing the Frobenius norm of the two signals. In particular, the Frobenius norm of the “measured” scattering matrix (Sij) is equal to 2.46 dB, while the one of the differential scattering matrix (ΔS) is -75.93 dB. This means that, the useful differential signal is about 80 dB below the measured one. Now, if we add to S_{ij} a Gaussian noise with $SNR = 90$ dB, and then perform the difference of the two noisy signals, the actual level of noise on ΔS is found to be such that $SNR = 9.5$ dB. In case of $SNR = 80$ dB on Sij, the SNR on ΔS turns to -0.5dB.

To show pictorially the entity of noise on the relevant signals, in Fig. 11 we report the absolute value of S_{1j} and ΔS_{1j}, i.e., the signals measured at the antennas when antenna one is probing, in absence and in presence of noise with $SNR = 80$ dB.

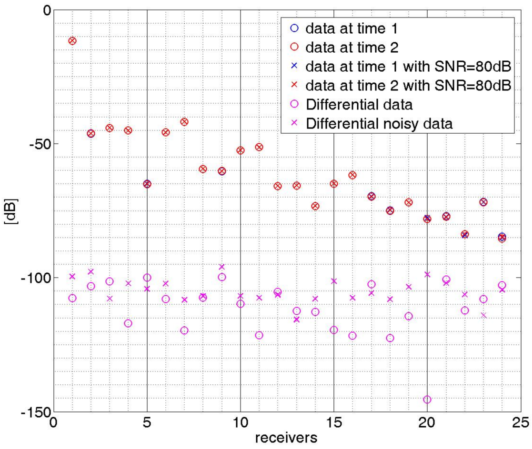

Fig. 11. Signals level obtained on all the receivers when one antenna is active.

It is also important to note that, while $SNR = 90$ dB is consistent with the design procedure carried out in previous section, an $SNR = 80$ dB means operating in worse conditions than the ones assumed in the design phase.

Figures 12 and 13 show the reconstructions obtained by means of the truncated SVD scheme for the stroke at position 1 and 2, respectively. As can be seen, the truncated SVD algorithm allows a satisfactory reconstruction of the perturbation inside a heterogeneous and complex head model, also in presence of the higher level of noise.

VI. CONCLUSIONS AND PERSPECTIVES

This paper presented the design of a low-complexity microwave imaging system for brain stroke monitoring. The design of the system was carried out by exploiting a recently proposed procedure, based on the mathematical properties of the relevant scattering operator. Moreover the working environment (operating frequency and coupling medium) have been set according to previous, experimentally validated, theoretical findings. Notably, the rigorous nature of the design approach has allowed to assess the obtained results in a quantitative fashion.

The result of this work is that a system for microwave brain stroke follow-up composed by 24 antennas evenly spaced on a helmet positioned at a distance of about 0.4λ, λ being the wavelength in the matching medium is a suitable candidate to fulfill the design constraints and pursue the sought imaging task.

Another important result of the analysis herein carried out is that, above all when dealing when real antennas in which coupling effects can play a not negligible noise, the dynamic range (and SNR) of the system is crucial in order to assure good reconstruction properties.

Future work is concerned with the realization of the system to pursue the monitoring goal for which the system has been designed on specifically developed anthropomorphic phantom [22] and using custom electronics [23]. In addition, efforts will be devoted to develop refined imaging strategies capable of providing high resolution imaging results. To this end, given the localized nature of the contrast distribution to be imaged, the adoption of regularization strategies aimed at promoting sparsity [24] is foreseen.

REFERENCES

[1] World health report. the world health report 2002 - reducing risks, promoting healthy life. [Online]. Available: http://www.who.int/whr/2002/en/

[2] S. Y. Semenov and D. R. Corfield, "Microwave tomography for brain imaging: feasibility assessment for stroke detection," *Int. J. of Antennas and Propagat.*, vol. 2008, p. 8 pages, 2008.

[3] S. Semenov, T. Huynh, T. Williams, B. Nicholson, and A. Vasilenko, "Dielectric properties of brain tissue in acute ischemic stroke: experimental study on swine," *Bioelectromagnetics*, vol. 38, pp. 158–163, 2017.

[4] M. Persson, A. Fhager, H. D. Trefnà, Y. Yu, T. McKelvey, G. Pegenius, J. E. Karlsson, and M. Elam, "Microwave-based stroke diagnosis making global prehospital thrombolytic treatment possible," *IEEE Transactions on Biomedical Engineering*, vol. 61, no. 11, pp. 2806–2817, Nov 2014.

[5] S. Candefjord, J. Winges, A. Malik, Y., Yu, T. Rylander, T. McKelvey, A. Fhager, M. Elam, and M. Persson, "Microwave technology for detecting traumatic intracranial bleedings: tests on phantom of subdural hematoma and numerical simulations," *Medical & Biological Engineering & Computing*, vol. 55, no. 8, pp. 1177–1188, Aug 2017.

[6] A. T. Mobashsher and A. M. Abbosh, "On-site rapid diagnosis of intracranial hematoma using portable multi-slice microwave imaging system," *Scientific Reports*, vol. 6, no. Article ID 37620, pp. 1–17, November 2016.

[7] A. T. Mobashsher, K. S. Bialkowski, A. M. Abbosh, and S. Crozier, "Design and experimental evaluation of a non-invasive microwave head imaging system for intracranial haemorrhage detection," *PLoS ONE*, vol. 11, no. 4, pp. 1–29, April 2016.

[8] M. Hopfer, R. Planas, A. Hamidipour, T. Henriksson, and S. Semenov, "Electromagnetic tomography for detection, differentiation, and monitoring of brain stroke: A virtual data and human head phantom study." *IEEE Antennas and Propagation Magazine*, vol. 59, no. 5, pp. 86–97, Oct 2017.

[9] R. Scapaticci, L. D. Donato, I. Catapano, and L. Crocco, "A feasibility study on Microwave Imaging for brain stroke monitoring," *Progress in Electromagnetics Research B*, vol. 40, pp. 305–324, 2012.

[10] R. Scapaticci, O. Bucci, I. Catapano, and L. Crocco, "Differential microwave imaging for brain stroke follow up," *International Journal of Antennas and Propagation*, vol. 2014, no. Article ID 312528, p. 11 pages, 2014.

[11] R. Scapaticci, M. Bjelogrlic, J. T. Vasquez, F. Vipiana, M. Mattes, and L. Crocco, *Emerging Electromagnetic Technologies for Brain Diseases Diagnostics, Monitoring and Therapy*. Springer int. pub., 2018, ch. 2. Microwave Technology for Brain Imaging and Monitoring: Physical Foundations, Potential and Limitations, pp. 7–35.

[12] O. M. Bucci, L. Crocco, R. Scapaticci, and G. Bellizzi, "On the design of phased arrays for medical applications," *Proceedings of the IEEE*, vol. 104, no. 3, pp. 633–648, March 2016.

[13] M. Bertero and P. Boccacci, *Introduction to Inverse Problems in Imaging*. Inst. Phys., Bristol, U.K., 1998.

[14] J. A. T. Vasquez, R. Scapaticci, G. Turvani, M. Vacca, I. Sarwar, M. R. Casu, G. Dassano, N. Joachimowicz, B. Duchêne, G. Bellizzi, E. Tedeschi, L. Crocco, and F. Vipiana, "A feasibility study for cerebrovascular diseases monitoring via microwave imaging," in *2017 International Conference on Electromagnetics in Advanced Applications (ICEAA)*, Sept 2017, pp. 1280–1282.

[15] S. Romeo, L. D. Donato, O. M. Bucci, I. Catapano, L. Crocco, M. R. Scarf, and R. Massa, "Dielectric characterization study of liquid-based materials for mimicking breast tissues," *Microw. Opt. Technol. Lett.*, vol. 53, pp. 1276 – 1280, 2011.

[16] N. Joachimowicz, C. Conessa, T. Henriksson, and B. Duchêne, "Breast phantoms for microwave imaging," *IEEE Antennas and Wireless Propagation Letters*, vol. 13, pp. 1333 – 1336, 2014.

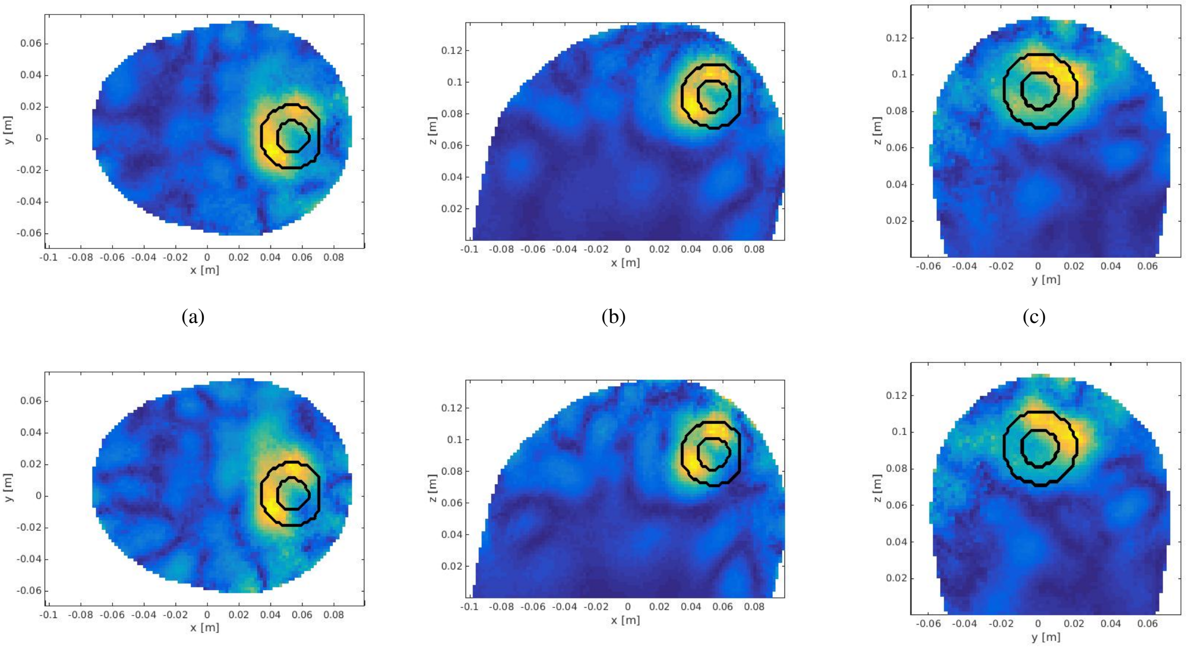

(a) (b) (c)

(d) (e) (f)

Fig. 12. Reconstructions along the three orthogonal body planes of the hemorrhage in position 1. On the top row reconstructions obtained with SNR = 90 dB; on the bottom row reconstructions obtained with SNR = 80 dB.

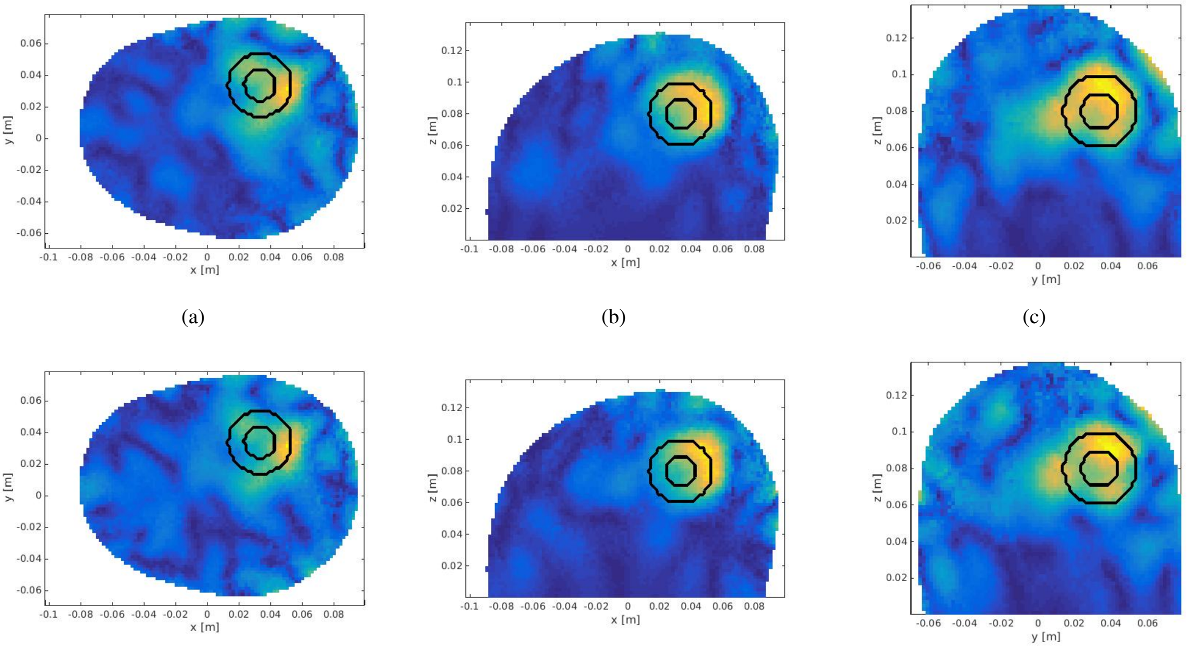

(a) (b) (c)

(d) (e) (f)

Fig. 13. Reconstruction along the three orthogonal body planes of the hemorrhage in position 2. On the top row reconstructions obtained with SNR = 90 dB; on the bottom row reconstructions obtained with SNR = 80 dB.

[17] O. M. Bucci, L. Crocco, and T. Isernia, “Improving the reconstruction capabilities in inverse scattering problems by exploitation of close-proximity setups,” *J. Opt. Soc. Am. A*, vol. 16, no. 7, pp. 1788–1798, Jul 1999.

[18] M. Slaney, A. C. Kak, and L. E. Larsen, “Limitations of imaging with first-order diffraction tomography,” *IEEE Transactions on Microwave Theory and Techniques*, vol. 32, no. 8, pp. 860–874, Aug 1984.

[19] S. N. Makarov, G. M. Noetscher, J. Yanamadala, M. W. Piazza, S. Louie, A. Prokop, A. Nazarian, and A. Nummenmaa, “Virtual human models for electromagnetic studies and their applications,” *IEEE Reviews in Biomedical Engineering*, vol. 10, pp. 95–121, 2017.

[20] D.Andreuccetti, R.Fossi, and C.Petrucci. An internet resource for the calculation of the dielectric properties of body tissues in the frequency range 10 hz - 100 ghz. ifac-cnr, florence (italy), 1997. based on data published by c.gabriel et al. in 1996. [Online]. Available: http://niremf.ifac.cnr.it/tissprop/

[21] E. A. Attardo, A. Borsic, G. Vecchi, and P. M. Meaney, “Whole-system electromagnetic modeling for microwave tomography,” *IEEE Antennas and Wireless Propagation Letters*, vol. 11, pp. 1618–1621, 2012.

[22] N. Joachimowicz, B. Duchêne, C. Conessa, and O. Meyer, “Reference phantoms for microwave imaging,” in *2017 11th European Conference on Antennas and Propagation (EUCAP)*, March 2017, pp. 2719–2722.

[23] M. R. Casu, M. Vacca, J. A. Tobon, A. Pulimeno, I. Sarwar, R. Solimene, and F. Vipiana, “A cots-based microwave imaging system for breast-cancer detection, ieee trans. on biomedical circuits and systems,” *IEEE Trans. on Biomedical Circuits and Systems*, vol. 11, no. 4, pp. 804–814, Aug. 2017.

[24] M. N. Stevanovic, R. Scapaticci, and L. Crocco, “Brain stroke monitoring using compressive sensing and higher order basis functions,” in *Antennas and Propagation (EUCAP), 2017 11th European Conference on*, Paris, France, 2017, pp. 2742–2745.